Humidity distribution affected by freely exposed water surfaces

Simulations and experimental verification

Hygum, Morten Arnfeldt; Popok, Vladimir

Published in:
Physical Review E. Statistical, Nonlinear, and Soft Matter Physics

DOI (link to publication from Publisher):
10.1103/PhysRevE.90.013023

Publication date:
2014

Document Version
Early version, also known as pre-print

Humidity distribution affected by freely exposed water surfaces: Simulations and experimental verification

M. A. Hygum* and V. N. Popok
Department of Physics and Nanotechnology, Aalborg University, Skjernvej 4a, 9220 Aalborg East, Denmark
(Received 27 March 2014; published 28 July 2014)

Accurate models for the water vapor flux at a water-air interface are required in various scientific, reliability and civil engineering aspects. Here, a study of humidity distribution in a container with air and freely exposed water is presented. A model predicting a spatial distribution and time evolution of relative humidity based on statistical rate theory and computational fluid dynamics is developed. In our approach we use short-term steady-state steps to simulate the slowly evolving evaporation in the system. Experiments demonstrate considerably good agreement with the computer modeling and allow one to distinguish the most important parameters for the model.

DOI: 10.1103/PhysRevE.90.013023 PACS number(s): 47.10.Fg, 05.70.Fh, 47.11.Fg

I. INTRODUCTION

One of the significant issues addressed by civil and reliability engineering is the problem of climatic simulations which very often includes the aspects of relative humidity (RH) of air affected by the presence of water. In particular, for electronic reliability engineering it is of importance to predict the humidity inside various enclosures. Some electronics operate outdoors and thus experience daily changes of temperature and humidity. It is hardly possible and quite expensive to make the boxes or cabinets completely hermetic. Therefore, changes in temperature and humidity can lead to water condensation and evaporation cycles which are dangerous for the electronics and can cause failures. Hence, the systems of interest here are containers in which a freely exposed water surface will give rise to an increase in the relative humidity of the air. The evaporation of water from the surface is thus not due to a boiling process but a desorption of the water molecules as a result of the interaction with gas molecules.

The adsorption and desorption processes of water molecules at water-air interfaces involve stochastic collisions of molecules in the gas and liquid phases, and therefore correspond to a rather complex problem.

There are three main approaches in order to deal with this problem. One of them is molecular dynamics (MD). An overview of this approach can be seen, e.g., in [1]. Another one, based on kinetic theory, is to solve the Boltzmann transport equation and obtain the velocity distribution function describing the system of interest. See [2,3] for a description of simulations based on kinetic theory. The third way is modeling based on irreversible thermodynamics where the basic principles of energy balance and a positive production of entropy at the interface are in use.

The MD approach attacks the problem at its fundamentals, i.e., molecules of different energies collide with water molecules at the surface. It has been used to investigate the mass fluxes at gas-liquid interfaces (see, e.g., [4] and [5]). It is computationally demanding, and therefore only fits to simulations of systems at the microscopic scale. However, MD simulations have been used to investigate the energy dependence of the condensation and evaporation coefficients [6]. These dependencies have been adapted to develop models for interfaces which are used as boundary conditions for direct simulation Monte Carlo methods [7].

Attempts to address the problem of water-air interfaces based on a macroscopic perspective have also been made. The Navier-Stokes and continuity equations are solved with particular source terms that take the vapor-liquid interfaces into account (see, e.g., [8]).

About two decades ago, Fang, Ward, and Stanga [9–11] showed that an air-water interface at steady-state evaporation and condensation conditions exhibits a relatively large temperature jump, on the order of a few degrees K. This result was in disagreement with the kinetic theory of evaporation and condensation. They developed an expression based on statistical rate theory (SRT) for the mass flux at a gas-liquid interface [10]. This development brought the model in good agreement with the temperature discontinuity and introduced a strong tool for computationally nonheavy simulations. Another advantage of SRT is in the absence of fitting parameters which makes the modeling more reliable.

In this paper a model which is based on the SRT approach suggested in [9–11] is developed. In contrast to the original usage of the expression we apply the model to slowly evolving dynamic systems using a number of sequent steady-state steps. By this approach, we are testing applicability of the model because to our best knowledge SRT expressions have not yet been used in computational fluid dynamics (CFD).

The developed model is utilized to predict the spatial RH distribution at room temperature in a container with liquid water. We verify the model experimentally and show the importance of taking convection processes into account.

II. THEORETICAL BASE FOR MODELING

This section presents some key equations important for understanding the developed model. The transport of water vapor can be modeled as movement of a diluted species in air. This is governed by the continuity equation [12]

$$\frac{\partial c(\vec{r},t)}{\partial t} + \vec{\nabla} \cdot \vec{J}(\vec{r},t) = Z(\vec{r},t), \tag{1}$$

where c is the concentration of water vapor, $\vec{r}$ is the position, and t is the time. $\vec{J}$ is the vapor flux and Z is the source term which represents the water surface. The flux term can be

*mah@nano.aau.dk

divided into diffusive and convective parts [12]:

$$\vec{J}(\vec{r},t) = -D_c\vec{\nabla}c(\vec{r},t) + c(\vec{r},t)\vec{u}(\vec{r},t), \tag{2}$$

with D_c to be the diffusion coefficient and $\vec{u}$ to be an Eulerian velocity field. Air is modeled as a slightly compressible fluid. The momentum conservation equation is given as

$$\rho\left[\frac{\partial\vec{u}}{\partial t} + (\vec{\nabla}\vec{u})\cdot\vec{u}\right] = -\vec{\nabla}p + \vec{\nabla}\cdot\tau + \vec{f}, \tag{3}$$

where p is the pressure, ρ is the density, and $\vec{f}$ is the body force due to gravity. It is worth mentioning that in some studies the nonlinear velocity term in Eq. (3) can be neglected, thus simplifying the calculations. However, as can be seen in Sec. III, in our case the flow gives rise to Reynolds numbers Re $\sim$ 30. Moreover, we investigate how the flow evolves to the steady state. These conditions do not allow one to disregard this term completely [12]. The viscous stress tensor is

$$\tau = \nu[\vec{\nabla}u + (\vec{\nabla}u)^T] - \tfrac{2}{3}\nu(\vec{\nabla}\cdot\vec{u})\mathbf{I} \tag{4}$$

with $\mathbf{I}$ to be the identity matrix and ν to be the dynamic viscosity [12]. The conservation of mass is governed by

$$\frac{\partial\rho}{\partial t} + \vec{\nabla}\cdot(\rho\vec{u}) = 0. \tag{5}$$

The calculation of the source term Z in Eq. (1) is based on the expression provided in [10]. Three central assumptions are made in order to derive the expression. The authors assume that the system of interest is at steady state and that the energy to maintain the temperature in the liquid is provided by the surroundings. It is also assumed that the condensation and evaporation coefficients are equal to unity. The following expression for the magnitude of molecular flux orthogonal to the water surface was developed [10]:

$$J_{\mathrm{SRT}} = K_e\left[\exp\left(\frac{\Delta S}{k_B}\right) - \exp\left(-\frac{\Delta S}{k_B}\right)\right]. \tag{6}$$

The first term is responsible for the evaporation and the second one for the condensation. The interfacial entropy change was shown to be

$$\Delta S = \left(\frac{\mu_l}{T_l} - \frac{\mu_v}{T_v}\right) + h_v\left(\frac{1}{T_v} - \frac{1}{T_l}\right), \tag{7}$$

where μ is the chemical potential, h is the enthalpy per molecule, and T is the temperature; all at the interface. The subscripts "l" and "v" denote liquid and vapor, respectively. The exchange rate K_e represents the rate at which molecules interact with the surface. It can be obtained by solving the Boltzmann transport equation for a system of a semi-infinite surface at steady state. An elaboration of this theory can be found in [13,14] and the exchange rate is given by

$$K_e = \frac{p_{v,e}}{\sqrt{2\pi m k_B T_l}}, \tag{8}$$

where m is the molecular mass and $p_{v,e}$ is the vapor pressure at equilibrium. This pressure can be rewritten using a particular reference for the chemical potential where it is the same for the molecules in the vapor and liquid phase [10]:

$$\mu_l(T_l, p_{\mathrm{sat}}(T_l)) = \mu_v(T_l, p_{\mathrm{sat}}(T_l)) = \mu(T_l, p_{\mathrm{sat}}(T_l)). \tag{9}$$

In this reference frame and under the assumption that the water is incompressible, the chemical potential can be given as

$$\mu_l(T_l, p_{l,e}) = \mu(T_l, p_{\mathrm{sat}}(T_l)) + V_l(p_{l,e} - p_{\mathrm{sat}}(T_l)), \tag{10}$$

with V_l to be the molar specific volume of the liquid. The chemical potential for the vapor, with the same reference state, is

$$\mu_v(T_v, p_{v,e}) = \mu(T_l, p_{\mathrm{sat}}(T_l)) + RT\,\ln\frac{p_{v,e}}{p_{\mathrm{sat}}(T_l)}, \tag{11}$$

where the vapor has been assumed to be ideal [10]. At equilibrium, the chemical potential on the left-hand side of Eqs. (10) and (11) are the same, which then gives rise to

$$p_{v,e} = \eta p_{\mathrm{sat}}(T_l), \tag{12}$$

where

$$\eta = e^{(V_l/V_v)\{[p_{l,e}/p_{\mathrm{sat}}(T_l)]-1\}}, \tag{13}$$

with V_v to be the molar specific volume of the vapor. It should be noticed that $V_v \gg V_l$ leading to $\eta \approx 1$ because $p_{l,e} \approx p_{\mathrm{sat}}$. p_l and p_v are connected by the Young-Laplace equation [12]:

$$p_l = p_v + \gamma\left(\frac{1}{r_1} + \frac{1}{r_2}\right), \tag{14}$$

where γ is the surface tension and r_1 and r_2 are the radii of curvature. As shown in [10] the entropy change can be given as

$$\begin{aligned}\Delta S = k_B\Bigg\{&4\left(1 - \frac{T_v}{T_l}\right) + \left(\frac{1}{T_v} - \frac{1}{T_l}\right)\\ &\times\sum_{l=1}^{3}\left(\frac{\hbar\omega_l}{2k_B} + \frac{\hbar\omega_l}{k_B e^{\hbar\omega_l/k_B T_v} - k_B}\right)\\ &+ \ln\left[\left(\frac{T_v}{T_l}\right)^4\left(\frac{p_{\mathrm{sat}}(T_l)}{p_v}\right)\right]\\ &+ \ln\left[\frac{q_{\mathrm{vib}}(T_v)}{q_{\mathrm{vib}}(T_l)}\right] + \frac{V_l}{k_B T_l}[p_l - p_{\mathrm{sat}}(T_l)]\Bigg\},\end{aligned} \tag{15}$$

where the vibrational partition function for the ideal polyatomic molecules, which in this case is water, may be expressed as

$$q_{\mathrm{vib}}(T) = \prod_{l=1}^{3}\frac{e^{-\hbar\omega_l/2k_B T}}{1 - e^{-\hbar\omega_l/k_B T}}. \tag{16}$$

The vibrational frequencies of the covalent bonds ω_l of a water molecule are 1590, 3651, and 3756 cm^{-1} [11].

III. SIMULATIONS

The simulations are carried out for the exact same geometry as the experimental setup has. This geometry is shown in Fig. 1 representing a cylinder with a water vessel (also of cylindrical shape) placed inside it. More details on the experimental setup can be found in the next section. To simulate RH inside the setup, the following issues are taken into account. The water surface of interest is relatively flat. Therefore, the curvature radii used in Eq. (14) are assumed to be so large that the pressure difference across the interface can be neglected.

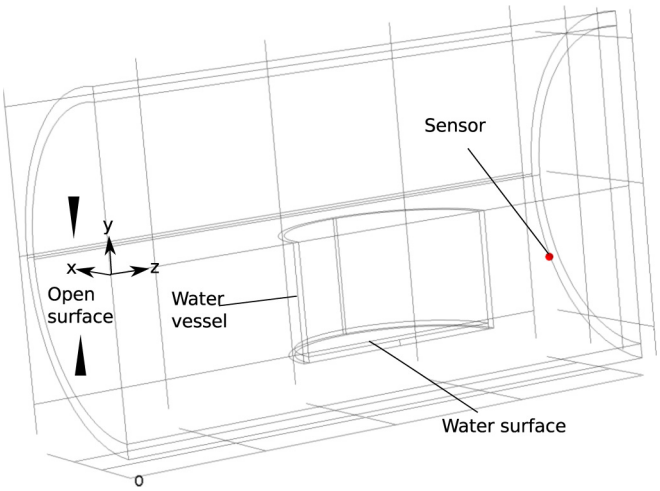

FIG. 1. (Color online) Schematic of the geometric model input.

Furthermore, the water level in the vessel is modeled to be constant due to the low evaporation rate on the time scales typically used in the simulations. This assumption follows from the experimental results described below. The water vapor is regarded as a diluted gas in air. The water surface represents a water vapor source, where a flux perpendicular to the surface is governed by Eq. (6). It was shown in [2] that steady-state evaporation from a planar water surface causes the temperature change only in the layer thinner than 1 cm above the water surface. Since the scale of our experimental setup is much larger, the temperature is assumed to be constant, $T = 293$ K. These simplifications significantly reduce the complexity of Eqs. (12) and (13). Furthermore, it enables Eq. (15) to be rewritten as

$$\frac{\Delta S}{k_B} = \ln\left(\frac{p_{\text{sat}}(T_l)}{p_v}\right) + \frac{V_l}{k_B T_l}[p_l - p_{\text{sat}}(T_l)]. \tag{17}$$

By comparison of the current equation with (15) it becomes obvious that the complexity is significantly reduced.

Water evaporation and change of RH in the cylinder is a dynamic but slowly evolving process. Therefore, we apply the so-called transient approach in which we divide the whole process into short time steps in which we consider the conditions to be the steady state. Thus, Eq. (6) can be applied for each time step. The transient solving procedure is then done by adaptive time stepping where the relative convergence tolerance is set to 10^{-4}.

All simulations were carried out using the finite element software COMSOL MULTIPHYSICS. RH given by

$$\theta = \frac{p_v}{p_{\text{sat}}} \tag{18}$$

has been modeled assuming the water vapor to be an ideal gas, hence

$$p_v = cRT, \tag{19}$$

where R is the ideal gas constant. The vapor concentration c follows Eq. (1) and $D_c = 2.4\times10^{-5}\frac{m^2}{s}$ at room temperature and atmospheric pressure according to [15]. The saturated water vapor pressure $p_{\text{sat}}(T) = 2.45$ kPa at $T = 293$ K [16].

TABLE I. Parameters used for viscosity calculation.

	$\nu_0(\frac{\text{Ns}}{\text{m}^2})$	T_0(K)	n_ν
ν_a	1.716×10^{-5}	273	0.666
ν_v	1.12×10^{-5}	350	1.15

The dynamic viscosity of humid air was obtained from [17] as

$$\nu_m = \sum_{i=1}^{2} \frac{X_i \nu_i}{\sum_{j=1}^{2} X_j \Phi_{ij}}, \tag{20}$$

where X_i is the mole fraction of air or water vapor (X_a for air and X_v for water vapor). The dynamic viscosity for air ν_a and water vapor ν_v are both obtained from

$$\nu_i = \nu_0\left(\frac{T}{T_0}\right)^{n_\nu}, \tag{21}$$

where the corresponding values of ν_0 and T_0 for air and water vapor are shown in Table I. Lastly,

$$\Phi_{ij} = \frac{1}{\sqrt{8}}\left(1+\frac{M_i}{M_j}\right)^{-1/2}\left[1+\sqrt{\frac{\nu_i}{\nu_j}}\left(\frac{M_j}{M_i}\right)^{1/4}\right]^2, \tag{22}$$

where M_i is the molar mass of the ith component.

To mimic RH at the open end of the cylinder the following concentration boundary is applied:

$$c_0 = 5.02\frac{\text{mol}}{\text{m}^3}, \tag{23}$$

which corresponds to a relative humidity of 50% at $T = 293$ K. This is the case when the humidity evolution is considered through the sheer diffusion.

However, one can suspect that the setup is not completely free of convection. Possible convection at the boundary is introduced as a downward flow with the velocity:

$$\vec{u}_0 = -u_0\frac{m}{s}\hat{\mathbf{y}}, \tag{24}$$

where the choice of the constant u_0 will be elaborated in Sec. V. The water vapor flux at the water surface is obtained by combining Eqs. (6), (8), and (17).

The simulation is carried out using the CFD and chemical species transport modules within COMSOL with an adaptive time stepper. With the boundary conditions used for the

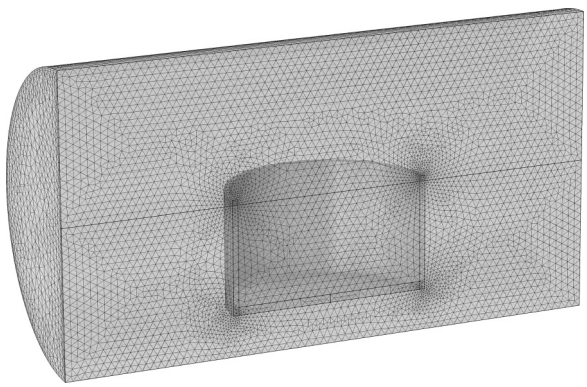

FIG. 2. Mesh used for the simulation of the setup containing the large water vessel.

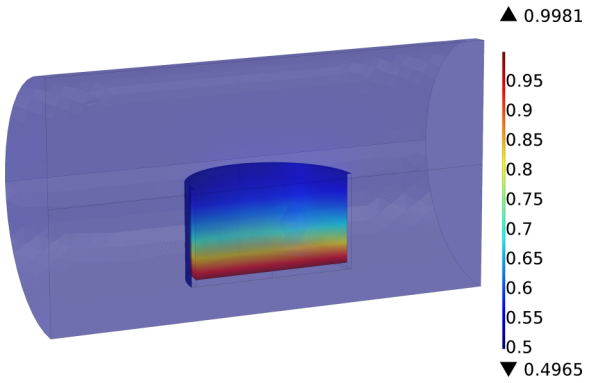

FIG. 3. (Color online) Initial profile of the relative humidity for the simulation with a large water vessel. Color scale shows RH.

velocity in this study, Reynolds number is found to be Re $\sim$ 30, thus corresponding to a laminar flow regime. Due to the symmetry, only half of the cylindrical setup is modeled as shown in Fig. 1. The velocity profile is obtained by solving Eq. (3) together with (4) and (5). For the pressure-velocity coupling a so-called projection method is used [18,19]. The continuity equation for the water vapor (1) is combined with Eqs. (2), (6), and (17) and iteratively solved at every time step.

The mesh was generated using COMSOL. For the simulation of the setup with the large vessel a total number of 631 940 elements is used. The mesh is shown in Fig. 2. For the simulation with the small water vessel the total number of elements is reduced to 494 643. The reason for the larger number of elements used in the simulation for the large vessel is to have the same mesh density at the evaporation areas for the large and small vessels.

An initial RH profile with still standing air is shown in Fig. 3.

IV. EXPERIMENT

The setup consists of a cylindrical tube made of Pyrex glass attached to an aluminum plate and tightened with rubber gaskets. The plate has an electrical feedthrough for connection of a temperature and humidity sensor. The cylinder is 20 cm long and has a radius of 5.5 cm. A schematic of the setup can be seen in Fig. 4.

The setup is placed in a clean room with well controlled surrounding temperature of 293 $\pm$ 0.5 K and RH of 49%–51%. A sensor is placed inside the setup to control the temperature and humidity. The sensor is Sensirion SHT75 which covers the temperature range from 233 to 373 K and the RH range from 0% to 100% with a maximum uncertainty of $\pm$5%.

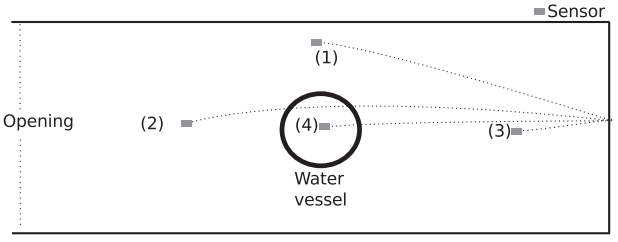

FIG. 4. Schematic top view of the experimental setup.

Prior to the experiments, readings of the sensor placed in the setup were compared with that of another sensor located outside. If the difference was greater than 5%, the sensor inside the setup was calibrated using the standard procedure recommended by the manufacturer.

Two kinds of experiments were conducted. The first series is referred to as flux experiments. A glass vessel with 10 ml of milli-Q water (T = 273 K) was put in the middle of the cylinder and the open side was tightly covered by a linen napkin to block convection. This napkin (Valusorb from Berkshire) is made of nonwoven polyester and cellulose and it has a structure with linear bundles of curled fibers. It is proven to be highly permeable to humid air but it should efficiently block convection due to the fact that the gaps in the napkin are on the micrometer scale. The amount of water evaporated from a vessel for a given time was measured by weighing the vessel before and after the experiment. Then the flux of evaporation was calculated.

The second series was carried out by placing a vessel of milli-Q water in the middle of the cylinder, tightly covering the open side by a linen napkin and monitoring the RH inside the setup until the steady state was reached. Again, the water temperature was 293 K. The spatial distribution of RH inside the setup was mapped by repeating such experiments with the humidity sensor placed at various locations.

Throughout both experimental series two water vessels were used. The large vessel has an inner radius of 3.5 cm and the small vessel has an inner radius of 2 cm.

RH was measured at 9 different positions inside the setup. In this paper we present the results for only four of them to avoid overloading with the similar experimental data and to focus on the most typical obtained dependencies. These positions can be seen in Fig. 4: (1) beside the vessel, (2) in front of vessel, (3) behind the vessel, and (4) above the vessel.

V. RESULTS AND DISCUSSION

A. Flux measurements and modeling

The measured fluxes and those modeled with the sheer diffusion are shown in Table II. The data presented in the experimental column are mean values obtained from three experiments with different times of evaporation which varied between 21 and 24 hours. As can be seen, the modeled values are smaller than the mean measured ones. However, the order of magnitude is the same. Taking into account that the fluxes are extremely small, one can conclude about good

TABLE II. Calculated fluxes using the approximation of sheer diffusion and experimentally measured fluxes. The fluxes have been calculated using Eq. (6), combined with Eqs. (8) and (17). Flux ratios between the small and large vessels are given for both model and experiment. The area ratio between the vessels is A = 0.33.

	Calculated flux	Measured flux
Small vessel	1.05×10^{-4} $\frac{\text{mol}}{\text{s m}^2}$	$(3.15\pm0.25)\times10^{-4}$ $\frac{\text{mol}}{\text{s m}^2}$
Large vessel	0.67×10^{-4} $\frac{\text{mol}}{\text{s m}^2}$	$(2.32\pm0.1)\times10^{-4}$ $\frac{\text{mol}}{\text{s m}^2}$
Flux ratio	1.57	1.36 ± 0.05

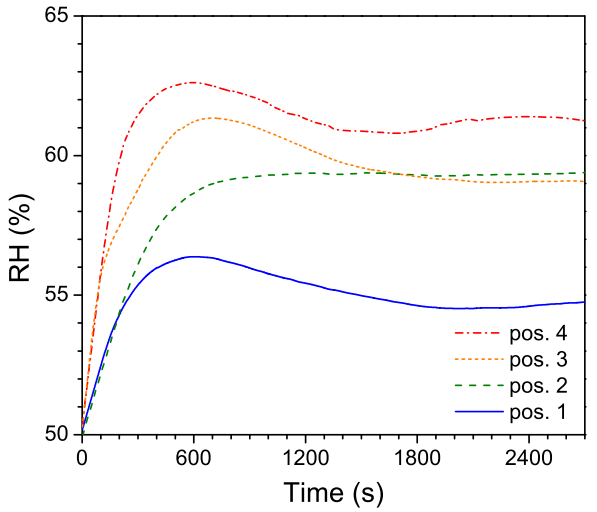

FIG. 5. (Color online) Change of RH with time for different sensor positions in the setup with the small vessel.

agreement between the simulations and the experiments. It is worth noting that in both model and experiment the flux is greater for the small vessel. This fact is related to the change in the configuration of the setup. The larger vessel takes up more space in the cylinder that changes the distribution of the surrounding water vapor and thus the flux is slightly reduced.

B. RH spatial distribution and time evolution

The measured changes of RH as a function of time are shown in Figs. 5 and 6 for the cases of small and large vessels, respectively. All the measurements reveal that RH reaches steady state after approximately 1800–2400 s. It is noticed that small bumps occur on the curves with maxima at around 500–600 s for both cases and sensor positions (1) and (3). These short-term increases of RH will be discussed later.

As a first step, simulations have been done with diffusion as the only transport mechanism, and a snapshot of a typical

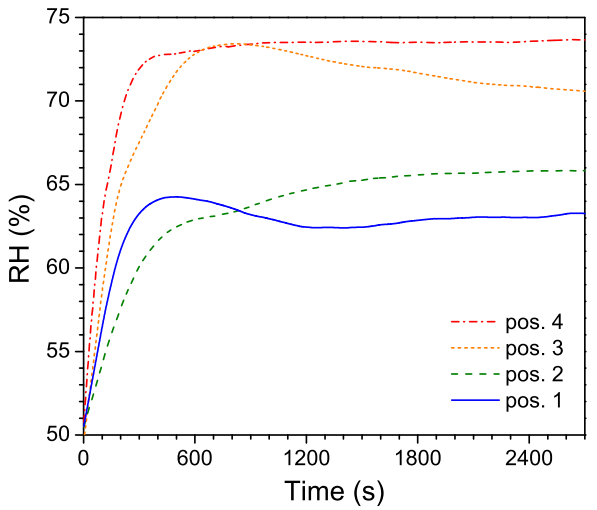

FIG. 6. (Color online) Change of RH with time for different sensor positions in the setup with the large vessel.

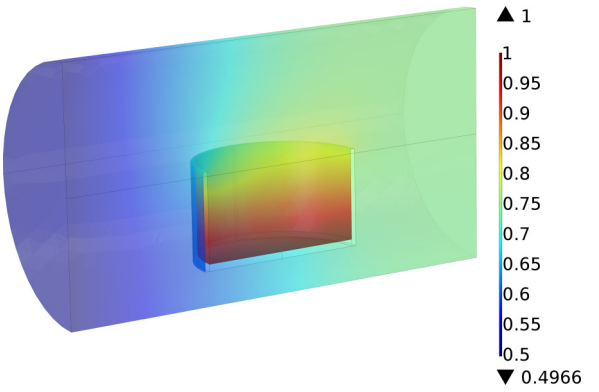

FIG. 7. (Color online) Simulated RH after 4000 s for the case of sheer diffusion with a large water vessel. Color scale shows RH.

RH profile 4000 s after putting the vessel with water into the setup is shown in Fig. 7. The time corresponds to steady state of RH in the entire cylinder. The snapshot shows that the humidity is highest just above the vessel. It is lower closer to the cylinder end wall and it is lowest near the open side covered by the napkin. These tendencies qualitatively agree with the experimental measurements. Comparisons between the measured and modeled RH on the time scale are shown in Figs. 8 and 9, where the error bars indicate the maximum measurement uncertainty provided by the sensor manufacturer. The comparison reveals that in the case of the small vessel the model gives a reasonable prediction of RH evolution for position (2): The simulated curve is within the error bars of the measurements. However, RH values are overestimated by the simulations on the long time scale for position (1). It is also clear that the model does not predict the appearance of the short-term increase of the RH, so-called bumps, at the initial stage of the experiment. Very similar tendencies are found in the case of the large vessel (see Fig. 9). For the nonshown sensor positions (3) and (4) the model also demonstrates

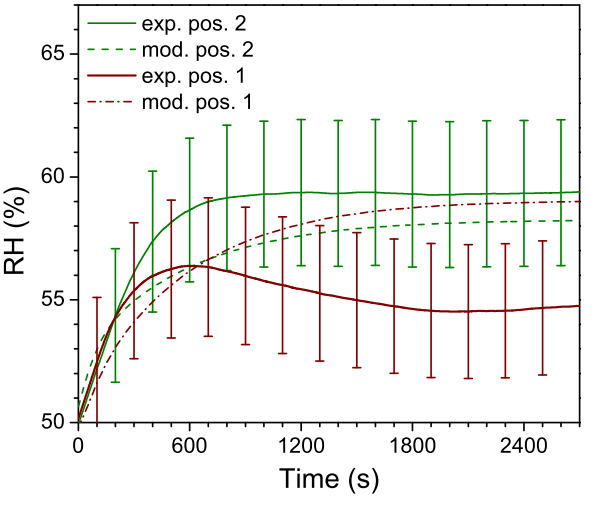

FIG. 8. (Color online) Experimental and modeled dependencies of RH on time for the setup with the small vessel and sensor positions (1) and (2). For the experimental curves, deviations due to the uncertainty of the sensor are shown as vertical bars.

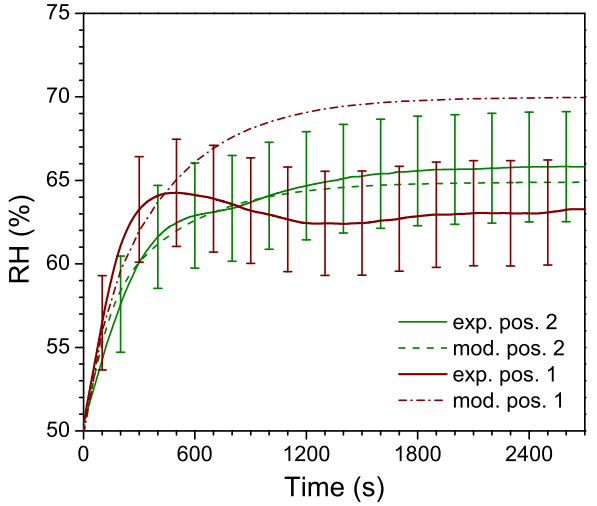

FIG. 9. (Color online) Experimental and modeled dependencies of RH on time for the setup with the large vessel and sensor positions (1) and (2). For the experimental curves, deviations due to the uncertainty of the sensor are shown as vertical bars.

only partial agreement with the experiment. Thus, one can conclude that the first simple model qualitatively predicts the RH distribution and time evolution in the setup but it probably misses some important phenomenon, which can be a convection term.

C. The role of convection

To test the role of convection and to improve the model, a boundary condition expressed by Eq. (24) is used. As an example, RH evolution is modeled for sensor position (1) and small vessel. For this case a few different values of u_0 were applied in Eq. (24) in order to investigate how convection affects the shape of the curves. The simulated evolutions of RH for three values of u_0 are presented in Fig. 10 for sensor position (2).

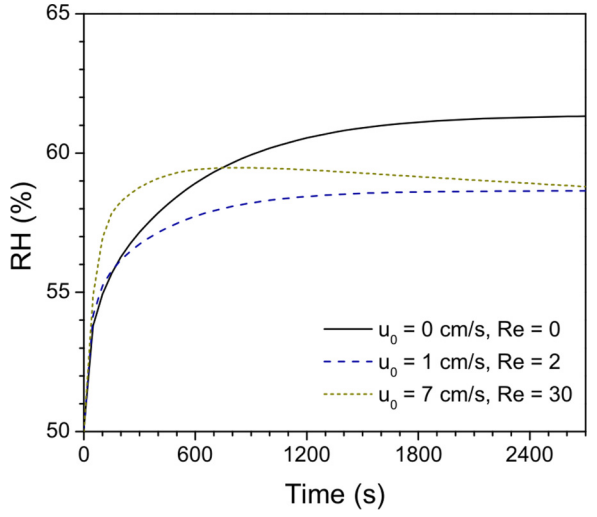

FIG. 10. (Color online) Modeled dependencies of RH on time for the cases of no convection ($u_0 = 0$ cm/s) and small convection velocities shown in the panel. The modeling is carried out for the setup with the small vessel at sensor position (2).

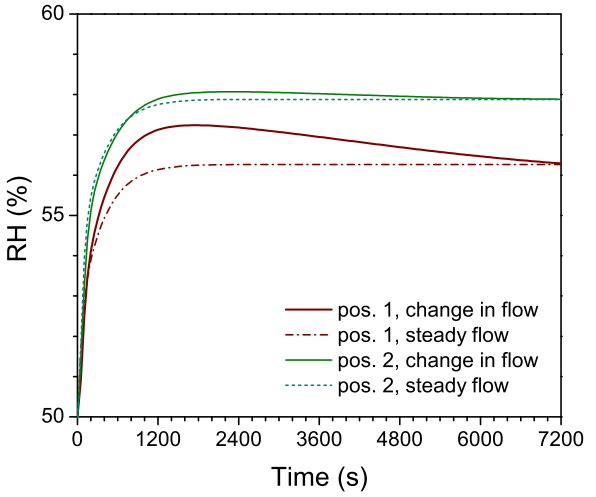

FIG. 11. (Color online) Modeled dependencies of RH on time for the case of convection with $u_0 = 2$ cm/s. For both sensor positions the simulation is done with time evolving (change in flow) and steady flows. See text for details.

First, the simulations show that adding even very small convection with $u_0 = 1$ cm/s corresponding to Re $= 2$ leads to a lowering of RH at the steady state. Second, further increase of the boundary velocity causes the appearance of a bump on the RH curve, thus, qualitatively reproducing the experimental measurements. Moreover, the initial rise of RH becomes much faster.

To get a better understanding of the physical reasons for the bumps on the humidity curves, two simulations for the case of the small vessel were done with $u_0 = 2$ cm/s (Re $= 17$). In the first simulation, the time evolution of RH is calculated using the assumption that the air is initially still in the cylinder but at $t = 0$ s the convection starts that leads to an evolving velocity profile until the steady-state velocity is reached. For the second simulation, the steady-state velocity profile obtained in the first simulation was used from the very beginning. The results of both simulations are presented in Fig. 11 for sensor positions (1) and (2). As seen in the figure, the first simulation is referred to as the time evolving flow and the second simulation as the steady-state flow.

One can see in Fig. 11 that the bumps occur only when a transient change in the air flow is present. By comparing these simulated curves with the experimental ones presented in Fig. 8 one can find good agreement in maximum and steady-state values of RH for both sensor positions. This allows one to conclude that the bumps are caused by convection introduced due to a short-term disturbance of air. This disturbance is assigned to the placement of the vessel inside the setup in the very beginning of the experiment causing unintentional movement of air which can include some nonlinear phenomena. It is worth noting that in the other series of experiments (not described here) the empty vessel placed in the setup was filled with water through a plastic pipe from outside thus minimizing possible unintentional air disturbances. In this case no bumps were observed, hence, proving our conclusion.

As one can see by comparing Figs. 11 and 8, the bump on the simulated curve is delayed with respect to the experimental one. Since it is hardly possible to measure the initial flow

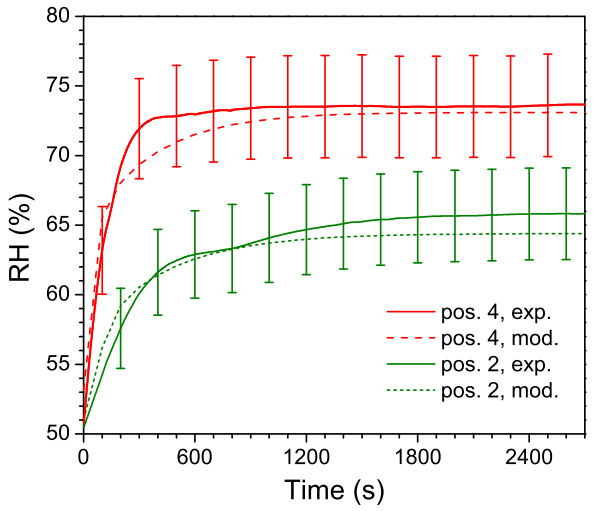

FIG. 12. (Color online) Experimental and modeled dependencies of RH on time for the setup with the large vessel. For the experimental curves, deviations due to the uncertainty of the sensor are shown as vertical bars. The simulated curves are based on the model including convection.

introduced by the moving vessel it cannot be expected that the model accurately predicts the bump appearances on the time scale.

By including convection and time evolving flow we also found good agreements between the simulations and experimental data on RH evolution for sensor positions (3) and (4) in the case of the small vessel as well as for all four positions in the case of the large vessel. In the simulations, the best agreement between the model and experiment was reached when the convection velocity was chosen to be between 1 and 2 cm/s. To demonstrate good agreement, a comparison of simulations and measurements for two sensor positions and the case of the large vessel is shown in Fig. 12. As one can see the model predicts the humidity evolution very accurately when the steady state is reached.

A snapshot of a typical, simulated RH profile in the setup with convection is shown in Fig. 13. The boundary condition $u_0 = 1$ cm/s. When comparing with the profile presented in Fig. 7 it can be noticed that the RH becomes more evenly distributed when convection is included in the model.

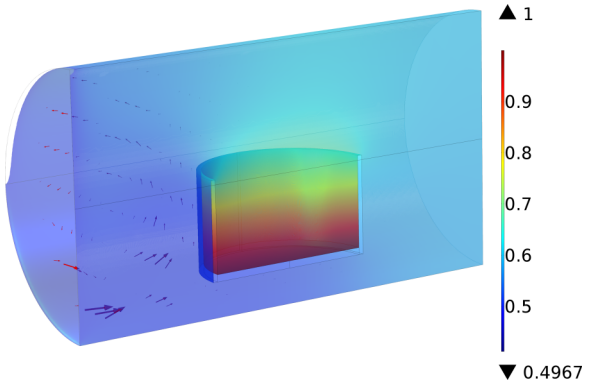

FIG. 13. (Color online) Simulated RH after 4000 s with $u_0 = 1$ cm/s for the case of the setup with the large water vessel. Color scale shows RH and the arrows indicate air flow.

TABLE III. Calculated fluxes and experimentally measured fluxes. The calculations include the slow convection process as discussed in the text. The fluxes have been calculated using Eq. (6), combined with Eqs. (8) and (17).

	Calculated flux	Measured flux
Small vessel	$1.17\times10^{-4}\ \frac{\text{mol}}{\text{s m}^2}$	$(3.15\pm0.25)\times10^{-4}\ \frac{\text{mol}}{\text{s m}^2}$
Large vessel	$0.89\times10^{-4}\ \frac{\text{mol}}{\text{s m}^2}$	$(2.32\pm0.1)\times10^{-4}\ \frac{\text{mol}}{\text{s m}^2}$
Flux ratio	1.31	1.36 ± 0.05

Adding the convection to the simulations also requires corrections of the water evaporation flux. New calculated data are presented in Table III showing better agreement with the experiment. There is still a difference between the modeled and the measured fluxes but one can see that the simulated and measured ratio values become the same within the standard deviations interval.

VI. CONCLUSION

We have studied relative humidity distribution in a simple cylindrical setup filled with air and containing a vessel with freely exposed water. This system imitates a box or cabinet at outdoor conditions in which the previously condensed water affects the spatial humidity profile through evaporation. This is a simplified model system which is of interest for reliability engineering. The spatial humidity distribution is studied both experimentally and theoretically.

In the experiments the flux of water evaporated from a vessel is measured and found to be small, on the order of $10^{-4}\frac{\text{mol}}{\text{s m}^2}$. Thus, the relative humidity increase due to the evaporation can be considered to be a dynamical but slowly evolving process. The change in RH and its time evolution is obtained at different sensor positions in the setup and for two configurations with the water vessels of different sizes. Experimental data are compared with the modeling. The model for simulation of spatial humidity distribution is based on statistical rate theory and computational fluid dynamics. It utilizes macroscopic quantities and the modeling is carried out by simultaneous solving of the Navies-Stokes and continuity equations for the water vapor. In our approach we use SRT for a number of sequent short-term steady-state time steps to simulate a slowly evolving dynamic system. The model is developed in two stages. At the first stage the diffusion is considered to be the only transport mechanism for the water vapor. This allows one to reach qualitative agreement with the experimental results but the model fails to predict correct RH values at the steady state and the effect of short-term rise of the humidity in the beginning of the experiment. The second stage introduces convection as an additional transport phenomenon, and thus significantly improves the model. One can conclude about its suitability for the prediction of RH spatial profiles in containers with simple geometry. Moreover, by including and tuning the convective flow one can further develop the approach towards modeling of more complex geometries, for instance containers with openings, and thus coming closer to the systems of practical engineering interest.

ACKNOWLEDGMENTS

This work is a part of research activities within the Center of Reliable Power Electronics (CORPE) funded by the Danish Strategic Research Council. We would like to acknowledge the company Grundfos for providing the experimental setup. We would also like to thank Jens Peter Krog from Grundfos and Dietmar Weiss from Danfoss for useful comments on the manuscript.

[1] R. Meland, A. Frezzotti, T. Ytrehus, and B. Hafskjold, Phys. Fluids **16**, 223 (2004).
[2] M. Bond and H. Struchtrup, Phys. Rev. E **70**, 061605 (2004).
[3] T. Ytrehus and S. Østmo, Int. J. Multiphase Flow **22**, 133 (1996).
[4] S. Cheng, J. B. Lechman, S. J. Plimpton, and G. S. Grest, J. Chem. Phys. **134**, 224704 (2011).
[5] K. Yasuoka, M. Matsumoto, and Y. Kataoka, J. Chem. Phys. **101**, 7904 (1994).
[6] T. Tsuruta, H. Tanaka, and T. Masuoka, Int. J. Heat Mass Transfer **42**, 4107 (1999).
[7] J. Caputa and H. Struchtrup, Physica A **390**, 31 (2011).
[8] S. Hardt and F. Wondra, J. Comput. Phys. **227**, 5871 (2008).
[9] G. Fang and C. A. Ward, Phys. Rev. E **59**, 417 (1999).
[10] C. A. Ward and G. Fang, Phys. Rev. E **59**, 429 (1999).
[11] C. A. Ward and D. Stanga, Phys. Rev. E **64**, 051509 (2001).
[12] H. Bruus, *Theoretical Microfluidics*, Oxford Master Series in Physics (Oxford University Press, Oxford, 2008).
[13] S. Chapman and T. Cowling, *The Mathematical Theory of Non-Uniform Gases: An Account of the Kinetic Theory of Viscosity, Thermal Conduction and Diffusion in Gases*, Cambridge Mathematical Library (Cambridge University Press, Cambridge, 1970).
[14] A. Kapoor and J. A. Elliott, J. Phys. Chem. B **112**, 15005 (2008).
[15] T. Marrero and E. A. Mason, J. Phys. Chem. Ref. Data **1**, 3 (1972).
[16] R. Weast and M. J. Astle, *CRC Handbook of Chemistry and Physics: A Ready Reference Book of Chemical and Physical Data* (CRC Press, Boca Raton, FL, 2013).
[17] J. Zhang, A. Gupta, and J. Baker, Heat Transfer Eng. **28**, 335 (2007).
[18] *COMSOL Multiphysics: Version 4.3b. User's Guide* (Comsol, 2013).
[19] J. Guermond, P. Minev, and J. Shen, Comput. Methods Appl. Mech. Eng. **195**, 6011 (2006).